JACS
JOURNAL OF THE AMERICAN CHEMICAL SOCIETY

Article

pubs.acs.org/JACS

Rational Design of Multilayer Collagen Nanosheets with Compositional and Structural Control

Tao Jiang,[†] Owen A. Vail,[‡] Zhigang Jiang,[‡] Xiaobing Zuo,[§] and Vincent P. Conticello*[,†]

[†]Department of Chemistry, Emory University, Atlanta, Georgia 30322, United States

[‡]School of Physics, Georgia Institute of Technology, Atlanta, Georgia 30332, United States

[§]X-ray Science Division, Argonne National Laboratory, 9700 South Cass Avenue, Argonne, Illinois 60439, United States

Supporting Information

ABSTRACT: Two collagen-mimetic peptides, **CP**$^+$ and **CP**$^-$, are reported in which the sequences comprise a multiblock architecture having positively charged N-terminal $(Pro\text{-}Arg\text{-}Gly)_3$ and negatively charged C-terminal $(Glu\text{-}Hyp\text{-}Gly)_3$ triad extensions, respectively. **CP**$^+$ rapidly self-associates into positively charged nanosheets based on a monolayer structure. In contrast, **CP**$^-$ self-assembles to form negatively charged monolayer nanosheets at a much slower rate, which can be accelerated in the presence of calcium(II) ion. A 2:1 mixture of unassociated **CP**$^-$ peptide with preformed **CP**$^+$ nanosheets generates structurally defined triple-layer nanosheets in which two **CP**$^-$ monolayers have formed on the identical surfaces of the **CP**$^+$ nanosheet template. Experimental data from electrostatic force microscopy (EFM) image analysis, zeta potential measurements, and charged nanoparticle binding assays support a negative surface charge state for the triple-layer nanosheets, which is the reverse of the positive surface charge state observed for the **CP**$^+$ monolayer nanosheets. The electrostatic complementarity between the **CP**$^+$ and **CP**$^-$ triple helical cohesive ends at the layer interfaces promotes a (**CP**$^-$/**CP**$^+$/**CP**$^-$) compositional gradient along the *z*-direction of the nanosheet. This structurally informed approach represents an attractive strategy for the fabrication of two-dimensional nanostructures with compositional control.

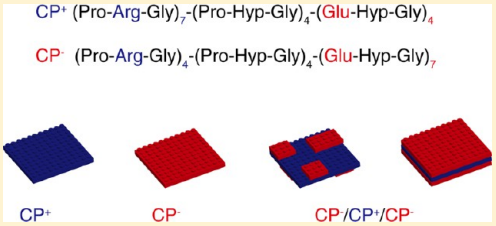

INTRODUCTION

The self-assembly of peptides,[1−9] proteins,[10] and architecturally related foldamers[11] has recently emerged as a method to create structurally defined and physically robust two-dimensional (2D) nanoscale assemblies (i.e., nanosheets). In several of these cases,[1,10,12] structural information derived from biophysical analysis of the nanosheets was employed to guide the design of functionalized assemblies in which the surfaces were modified selectively with exogenous substrates. This nanoarchitectonic approach[13,14] holds significant promise for the fabrication of functional nanosheet assemblies for technological applications. In order to develop these nanosheets as platforms for integration into more complex structures, uniform populations of structurally and dimensionally defined sheets would be the optimal starting point. Thus far, however, the composition of these nanosheets has been limited to homogeneous populations of protomers with little control over growth in the lateral (x/y) or vertical (z) directions. We report herein the design of protomers derived from collagen-mimetic peptides (**CMPs**) in which self-assembly can be directed selectively toward the formation of multilayer structures of defined composition and surface chemistry.

Recently, we reported the fabrication of nanosheets from self-assembly of a series of collagen-mimetic peptides: **NSI**, **NSII**, and **NSIII**.[1,2] The sequences of these peptides comprised three consecutive blocks of positively charged, neutral, and negatively charged (Xaa-Yaa-Gly) triads arranged in order from the N-terminus to the C-terminus of the respective peptides. Structural analysis of the nanosheets was consistent with a model based on a tetragonal 2D lattice, in which structurally adjacent triple helices were packed in an antiparallel arrangement. The long axes of the triple helices displayed a perpendicular orientation with respect to the sheet surface such that the length of the triple helix defined the thickness of a layer within the nanosheet. Coulombic interactions between the positively charged amino acids in the first block and the negatively charged residues of the third block ostensibly provided the thermodynamic driving force for nanosheet self-assembly. However, striking differences in self-assembly behavior were observed between the structurally related peptides within this series. The **NSI** and **NSII** nanosheets were highly polymorphic in the lateral (x/y) directions, with **NSI** nanosheets also displaying polymorphism in the vertical (z) direction. In contrast, the **NSIII** nanosheets were very uniform in lateral dimension and exclusively displayed single-layer thickness.

The mechanism responsible for the differences in nanosheet morphology was difficult to deconvolute due to the absence of structural information on the assemblies at atomic-level resolution. Moreover, the positively charged amino acids within this peptide series corresponded to either (4*R*)- or (4*S*)-4-aminoproline. The conformational behavior of these non-canonical imino acid derivatives within the structural context of

Received: March 30, 2015
Published: May 28, 2015

DOI: 10.1021/jacs.5b03326
J. Am. Chem. Soc. 2015, 137, 7793−7802

the collagen triple helix has been shown to be a complex function of pH and sequence position.[15,16] In addition, the influence of these aminoproline derivatives on protein structure is only beginning to be understood at the molecular level.[17,18] At this point in time, these considerations limit the utility of the peptides within the **NS** series as substrates for the development of a broadly applicable nanoscale structural platform.

Previously, we reported the design of a collagen-mimetic peptide **CPII** (Figure 1), which self-assembled from aqueous

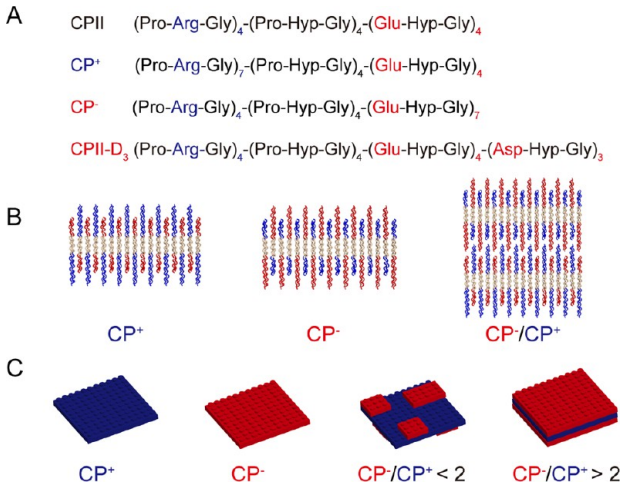

Figure 1. (A) Amino acid sequences of peptides employed in this study. (B) Side view of the proposed antiparallel packing of triple helices within individual layers and a stacked bilayer. Individual lines represent triple helices with different charged blocks. (C) Three-dimensional representations of charged nanosheet assemblies from $\mathbf{CP}^+$ and $\mathbf{CP}^-$ peptides, and multilayer structures at different $\mathbf{CP}^-/\mathbf{CP}^+$ mixing ratios. Color code for amino acid residues, helices, and surfaces: red, negatively charged; neutral, uncharged; blue, positively charged.

solution into banded fibrils.[19] However, under appropriate conditions, **CPII** was also observed to form nanosheet structures similar to those derived from peptides within the **NS** series (Figure S1, Supporting Information).[1] In contrast to the **NS** peptides, the sequence of **CPII** encompassed charged amino acid residues that occur frequently in native collagen isoforms.[20] In addition, the nature of electrostatic interactions between oppositely charged canonical amino acids within the collagen triple helix[21] are reasonably well understood from structural analyses of model peptide systems,[22−24] including those that self-assemble into structurally ordered materials.[19,25,26] On this basis, **CPII** peptide derivatives represent more attractive substrates for the controlled fabrication of nanosheet assemblies and may serve as a valuable test bed for examination of the influence of different architectural features on the self-assembly of the corresponding nanosheets.

The self-assembly of nanosheets based on collagen-mimetic peptides has been described in terms of a structural model in which the triple helix defines the layer thickness.[1,2] Structural analyses of the nanosheets have demonstrated that the peptide termini are displayed at the surface of the assembly.[1] In order to promote controlled growth in the *z*-direction, we rationalized that collagen-mimetic peptides that encompassed an asymmetric distribution of charged blocks might localize the uncompensated charge on the surface of the nanosheet after self-assembly (Figure 1). Peptide-based nanosheets with surface charges could be employed as a strategy to manipulate the *z*-directional sheet stacking preferences in order to promote the formation of multilayer structures. This process is conceptually analogous to "layer-by-layer adsorption",[27] which employs electrostatic attraction between oppositely charged polymers to build multicomponent systems of defined composition.

However, simple charge complementation may not be sufficient to guarantee the formation of multilayer nanosheet assemblies that display a high degree of internal structural order. In order to address this concern, the charged residues were incorporated within the structural context of collagen triad repeats. The charged triple helical extensions should localize at the surface of the resultant nanosheets and present a preorganized template for assembly of nanosheets derived from peptides having complementary sequences of charged triads (Figure 1). The surfaces of the nanosheets could be considered to resemble Lego plate assemblies at the supramolecular level, in that spatially defined patterns of studs and tubes occur at the interface between nanosheets due to the periodic arrangement of charged triple helical cohesive ends. The nascent layers should adopt the underlying 2D lattice structure of the nucleating nanosheet due to a template effect (Figure 1).

RESULTS AND DISCUSSION

In order to test this hypothesis, we designed and synthesized two peptides, $\mathbf{CP}^+$ and $\mathbf{CP}^-$, having asymmetric distributions of charged triad sequences (Figure 1A). The core sequence of each peptide is derived from **CPII**,[19] but extensions corresponding to three positively charged triads or negatively charged triads were added to the N-terminus of $\mathbf{CP}^+$ or C-terminus of $\mathbf{CP}^-$, respectively. These three extra triads should protrude from the surface of the nanosheet after self-assembly of the respective peptides. The identity of the positively charged triads (Pro-Arg-Gly) and negatively charged triads (Glu-Hyp-Gly) reflect positional preferences that were previously determined from host−guest studies of collagen-mimetic peptides.[28]

Circular dichroism (CD) spectropolarimetry was employed to assess the conformational properties of the $\mathbf{CP}^+$ and $\mathbf{CP}^-$ peptides in buffered aqueous solution, as well as the thermal stabilities of the resultant triple helices (Figure 2). $\mathbf{CP}^+$ and $\mathbf{CP}^-$ peptides (1 mg/mL) in MES buffer (20 mM, pH 6.0) displayed the classic CD signature of a collagen-like triple helix, with a maximum absorption from 222 to 224 nm and a minimum absorption from 195 to 199 nm. The melting transition (T_m) of peptide $\mathbf{CP}^+$ (68 °C) was observed to be

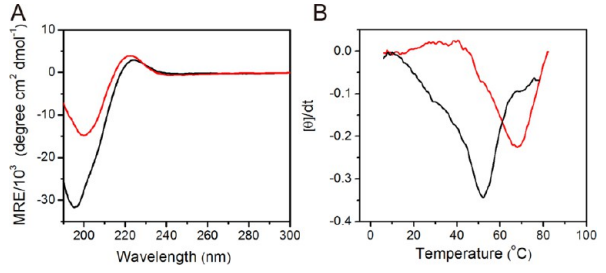

Figure 2. (A) CD spectra of peptides $\mathbf{CP}^+$ (red) and $\mathbf{CP}^-$ (black). (B) First derivative of the CD melting curves at 223 nm as a function of temperature. The melting temperatures were estimated from the minimum in the first derivative curves. CD spectra were measured for peptide solutions at a concentration of 1 mg/mL in MES buffer (20 mM, pH 6.0).

DOI: 10.1021/jacs.5b03326
J. Am. Chem. Soc. 2015, 137, 7793−7802

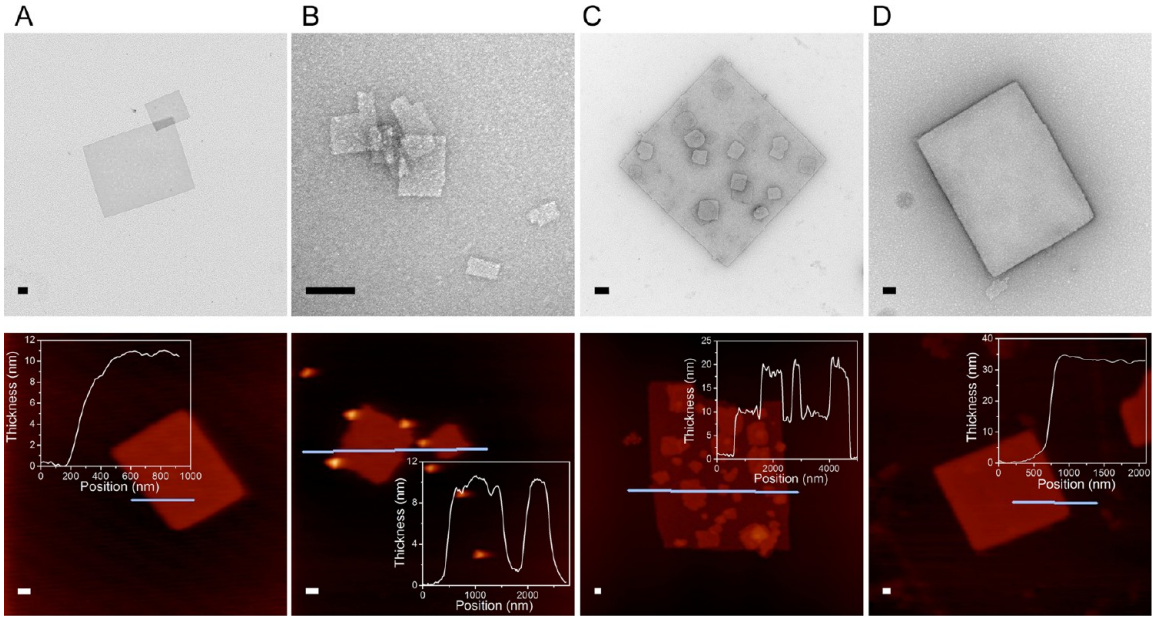

Figure 3. Representative TEM (upper) and tapping mode AFM images (lower) of (A) **CP**$^+$ nanosheets, (B) **CP**$^-$ nanosheets with Ca^{2+}, (C) mixed **CP**$^+$/**CP**$^-$ assemblies resulting from a **CP**$^-$/**CP**$^+$ concentration ratio of 1:5, and (D) mature multilayer assemblies from incubation of preformed **CP**$^+$ nanosheets with free **CP**$^-$ peptide at a **CP**$^-$:**CP**$^+$ concentration ratio of 2:1. All samples were assembled in MES buffer (20 mM, pH 6.0). Scale bars denote 200 nm.

significantly higher than the corresponding transition for **CP**$^-$ (52 °C). Notably, the T_m values for triple helices derived from either the **CP**$^+$ peptide or the **CP**$^-$ peptide were greater than the corresponding T_m value of 39 °C for the parent **CPII** system[19] under identical conditions (Figure S2, Supporting Information).

The trend in CD data can be understood in terms of the relative influence of the respective triads on the thermodynamic stability of triple helices derived from collagen-mimetic peptides.[28] The (Pro-Arg-Gly) triad was observed to be similar in stability to the canonical (Pro-Hyp-Gly) triad in host–guest model peptide systems.[29] The stabilizing effect of arginine at the Yaa position has been attributed to its potential for the formation of intramolecular or intermolecular hydrogen-bonding interactions in the structural context of a collagen triple helix.[29,30] In contrast, the (Glu-Hyp-Gly) triad, despite having the greatest stability among (Xaa-Hyp-Gly) guest triads, was nonetheless destabilizing vis-à-vis the canonical (Pro-Hyp-Gly) triad sequence. These observed T_m values for triple helices of **CP**$^+$ versus **CP**$^-$ can be attributed to the presence of a greater number of stabilizing (Pro-Arg-Gly) triads in the former peptide in comparison to the presence of destabilizing (Glu-Hyp-Gly) triads in the latter case.

Transmission electron microscopy (TEM) was employed to investigate the morphology of species derived from self-assembly of the **CP**$^+$ and **CP**$^-$ peptides (Figure 3A and B). Peptide **CP**$^+$ underwent self-assembly into nanosheet structures in MES buffer (20 mM, pH 6.0) over a period of hours, even at concentrations as low as 0.2 mg/mL. In contrast, peptide **CP**$^-$ formed detectable nanosheets only over a period of months at a concentration of ≥5 mg/mL in MES buffer (20 mM, pH 6.0). The addition of calcium(II) ion (4 mM, approximately a 1:1 ratio per excess Glu residue) was observed to accelerate the self-assembly of the **CP**$^-$ nanosheets (5 mg/mL), effectively lowering the association time from months to hours. Calcium-(II) ion can coordinate to glutamate residues within proteins,[31] often displaying K_d values in the μM to mM range within calcium binding proteins.[32] Coordination of calcium ion may stabilize the **CP**$^-$ assemblies through partial neutralization of the excess negative charge of the glutamate side chains within the $(Glu\text{-}Hyp\text{-}Gly)_3$ extensions. However, a comparison of the CD melting curves for **CP**$^-$ in the presence or absence of calcium(II) ion indicated an insignificant difference in T_m between the two samples (Figures S3 and S4, Supporting Information). These results suggest that the calcium ions probably promote self-assembly through coordination of glutamate residues on proximal triple helices within a nanosheet rather than stabilization of the triple helical conformation.

However, the slow self-assembly of the **CP**$^-$ nanosheets in the absence of calcium(II) ion cannot be solely attributed to the negative charge associated with the three extra (Glu-Hyp-Gly) triads. A variant peptide, **CP**$^-$**D**$_3$, in which the three C-terminal triads were replaced with (Asp-Hyp-Gly), could self-assemble into nanosheets within hours in the absence of calcium ion (Figure S5, Supporting Information). Notably, CD spectropolarimetry of the **CP**$^-$**D**$_3$ assemblies indicated a melting transition of ca. 60 °C, which is significantly greater than that of the parent peptide **CP**$^-$ (Figures S6 and S7, Supporting Information). Thus, the $(Asp\text{-}Hyp\text{-}Gly)_3$ triad extensions can stabilize the triple helix and promote nanosheet assembly, despite a weaker propensity for triple helix formation from model studies on host–guest peptides.[28] The difference in thermodynamic stability and kinetics of self-association between **CP**$^-$ and **CP**$^-$**D**$_3$ cannot be fully attributed to the small difference in pK_a between the Asp and Glu side chains ($\Delta pK_a \approx 0.2$) of the free amino acids. However, Asp residues have been observed to form hydrogen-bonded interactions with each other in the crystal structure of a collagen triple helix derived from a model peptide, which may provide a rationale for the observed differences in nanosheet formation between **CP**$^-$ and **CP**$^-$**D**$_3$.[33]

DOI: 10.1021/jacs.5b03326
J. Am. Chem. Soc. 2015, 137, 7793–7802

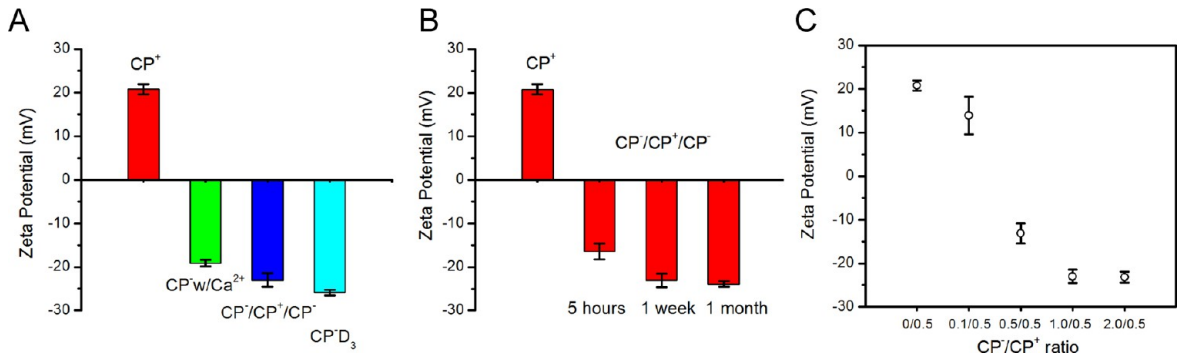

Figure 4. (A) Zeta potential measurements of solutions of $\mathbf{CP^+}$ nanosheets, $\mathbf{CP^-}$ nanosheets with Ca^{2+}, mature $\mathbf{CP^-/CP^+/CP^-}$ triple-layer nanosheets, and $\mathbf{CP^-D_3}$ nanosheets after 1 week of incubation. (B) Time dependence of the zeta potential for assemblies derived from incubation of preformed $\mathbf{CP^+}$ nanosheets with free $\mathbf{CP^-}$ peptide at a $\mathbf{CP^-}$:$\mathbf{CP^+}$ concentration ratio of 2:1. (C) Concentration dependence of the zeta potential for assemblies derived from incubation of preformed $\mathbf{CP^+}$ nanosheets with free $\mathbf{CP^-}$ peptide. Zeta potentials were measured at ambient temperature for nanosheet assemblies immediately after dilution to a concentration of 0.1 mg/mL in MES buffer (20 mM, pH 6.0).

A tapping mode atomic force microscope (AFM) was employed to estimate the thickness of nanosheets derived from self-assembly of the $\mathbf{CP^+}$ and the $\mathbf{CP^-}$ peptides in MES buffer (Figure 3A and B). The $\mathbf{CP^-}$ nanosheets (5 mg/mL) were assembled in the presence of calcium(II) ion (4 mM). Statistical analysis of the AFM height measurements (Figure S8, Supporting Information) indicated an average thickness of 9.4 ± 1.0 nm for the $\mathbf{CP^+}$ nanosheets and 9.9 ± 1.2 nm for the $\mathbf{CP^-}$ nanosheets. The theoretical monolayer thicknesses were calculated to be 10.3 nm for the structured core of a 2D layer derived from the **CPII** peptide sequence (36 residues × 0.286 nm rise/residue for collagen triple helices).[1,2,34] The calculated thickness of the structured core is within experimental error of the measured thicknesses for the respective nanosheet assemblies. The close correspondence of the values suggests that the triads extending from either surface of the assembly might be unstructured under the dry conditions employed for AFM measurements. Due to the proposed antiparallel arrangement of adjacent triple helices within the structure (*vide infra*), the charged extensions from structurally adjacent triple helices should protrude from opposite surfaces of the nanosheet (Figure 1). Consequently, in the absence of charge compensation from an oppositely charged triple helix, the extensions may be destabilized due to charge repulsion between similarly charged amino acid residues.

If indeed these extensions are accessible at the surface of the assemblies, they should be available to interact with oppositely charged triple helices and nucleate the formation of charge complementary layers on the exposed surfaces of the original nanosheet. Since the $\mathbf{CP^+}$ peptide assembled readily from buffered aqueous solution, the corresponding nanosheets were employed as a substrate to template the growth of nanosheets derived from the $\mathbf{CP^-}$ peptide. The morphologies of resultant structures depended on the initial concentration ratio of unassembled $\mathbf{CP^-}$ peptide with respect to the concentration of the $\mathbf{CP^+}$ peptide in the preformed nanosheets. At concentration ratios of less than 2:1 ($\mathbf{CP^-}$:$\mathbf{CP^+}$), layered structures were observed that appeared as small sheets located on the surface of larger preassembled $\mathbf{CP^+}$ nanosheets (Figure 3C). At a stoichiometric ratio of $\mathbf{CP^-}$:$\mathbf{CP^+}$ ≥ 2:1, the nascent nanosheets on the surface of the basal nanosheet were observed to fuse into a single continuous layer that extended over the entire surface of the original nanosheet (Figure 3D). This controlled growth of nanosheets in the *z*-direction contrasts with the uncontrolled sheet stacking observed for the parent peptide **CPII** (Figure S1, Supporting Information). These results suggest that the presence of the charged overhangs prevents association between similarly charged nanosheets, as expected on the basis of electrostatic considerations.

AFM height measurements of the partially formed nanosheets, assembled at lower $\mathbf{CP^-}$:$\mathbf{CP^+}$ concentration ratios (Figure 3C), indicated that both the nascent layers and the original nanosheet had thickness values of ca. 10 nm, which correlated well with the previously observed height values for the individual monolayer nanosheets. AFM height measurements on the mature nanosheets indicated an average height of 34 ± 2.0 nm (Figure 3D). These height measurements were in agreement with a calculated thickness of 36 nm for a theoretical model consisting of a triple-layer nanosheet (3 × 10.3 nm core layers with two structured intersheet regions of 9 residues × 0.286 nm rise/residue). This model for sheet growth is consistent with the proposed antiparallel orientation of adjacent triple helices within the collagen-based nanosheets,[1,2] which necessitates that the two surfaces are identical and, therefore, equally competent to promote the growth of new layers. Notably, each of the individual peptides can only support the growth of single-layer nanosheets in isolation, which is presumably a consequence of the high charge density at the surface of the individual nanosheets. Full surface coverage is only observed under conditions in which the concentration ratio of $\mathbf{CP^-}$:$\mathbf{CP^+}$ is ≥2:1, which would be a prerequisite for the formation of a triple-layer structure with full surface coverage.

An important consequence of this proposed mechanism is that the surface charge of the triple-layer structure should be opposite to that of the original nanosheet structure. The preformed $\mathbf{CP^+}$ nanosheet should display a positive surface charge due to the presence of the N-terminal $(\text{Pro-Arg-Gly})_3$ extensions. Since the growth of the triple-layered structure involves lamination with the oppositely charged $\mathbf{CP^-}$ peptide, the corresponding nanosheets should display a negative surface charge due to the presence of the C-terminal $(\text{Glu-Hyp-Gly})_3$ extensions.

Zeta potentials were determined for individual nanosheets as well as the mature triple-layered nanosheets (Figure 4). The zeta potential of the $\mathbf{CP^+}$ nanosheets (0.1 mg/mL) was measured to be ca. +20 mV, and that of the $\mathbf{CP^-}$ sheets (0.1 mg/mL, 0.08 mM Ca^{2+}) was ca. −19 mV. As a control, $\mathbf{CP^-D_3}$ nanosheets had an observed zeta potential of ca. −26 mV (Figure 4A). These results are in agreement with the assumption that the arginine containing extensions confer a

DOI: 10.1021/jacs.5b03326
J. Am. Chem. Soc. 2015, 137, 7793−7802

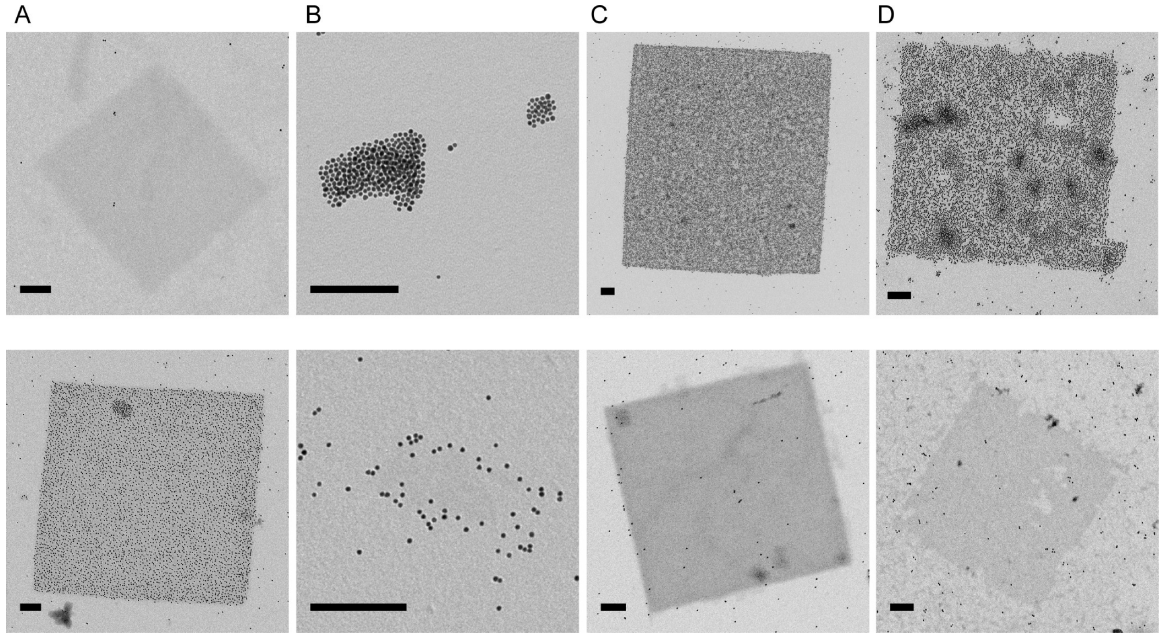

Figure 5. TEM images of unstained peptide nanosheets probed with cationic (upper row) and anionic (lower row) gold nanoparticles from (A) **CP**$^+$ nanosheets, (B) **CP**$^-$ nanosheets with Ca^{2+}, (C) mature **CP**$^-$/**CP**$^+$/**CP**$^-$ triple-layer nanosheets, and (D) **CP**$^-$**D**$_3$ nanosheets. Scale bars are 200 nm.

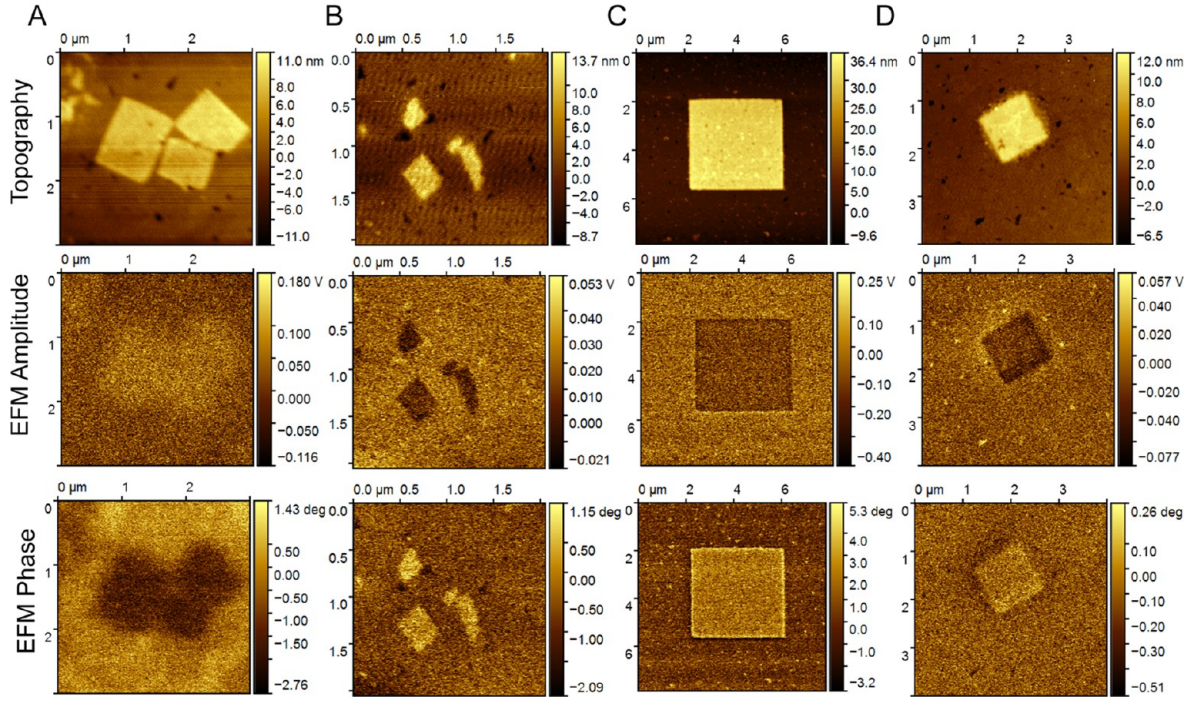

Figure 6. AFM topographic (upper row), EFM amplitude (middle row), and EFM phase (lower row) images of nanosheet specimens: (A) **CP**$^+$ nanosheets; (B) **CP**$^-$ nanosheets with Ca^{2+}; (C) multilayer (**CP**$^-$/**CP**$^+$/**CP**$^-$) nanosheets; (D) **CP**$^-$**D**$_3$ nanosheets. EFM amplitude and phase images were mapped with a tip bias of +2 V.

positive surface charge to the **CP**$^+$ nanosheets, whereas the glutamate or aspartate extensions provide negative surface charges to **CP**$^-$ and **CP**$^-$**D**$_3$ nanosheets. When adding the unassembled **CP**$^-$ peptide to preformed **CP**$^+$ nanosheets in the concentration ratio of 2:1, the zeta potentials of the resultant structures decreased to negative values within hours and stabilized to ca. −23 mV after 1 week of incubation (Figure 4B). For mixtures of the **CP**$^-$/**CP**$^+$ peptides at different concentration ratios, the zeta potentials of the corresponding structures decreased as the concentration ratio of the peptides increased until it reached the limiting value of 2:1 (Figure 4C). The zeta potential measurements strongly support a triple-layered model in which growth of negatively charged layers occurs on the top and bottom surfaces of the original positively charged nanosheet.

In order to correlate surface charge with nanosheet topology, two complementary methods were investigated. In the first case, gold nanoparticles with charged surface layers were

DOI: 10.1021/jacs.5b03326
J. Am. Chem. Soc. 2015, 137, 7793−7802

employed as probes to distinguish among the nanosheets on the basis of differential adsorption. These measurements were predicated on the assumption that the excess charged residues on the surfaces of the nanosheets would be accessible for interaction with oppositely charged gold nanoparticles.[1] Unstained sheets were probed with either cationic gold nanoparticles (10 nm core functionalized with (11-mercaptoundecyl)-*N*,*N*,*N*-trimethylammonium bromide) or anionic gold nanoparticles (9 nm core labeled with mercaptopoly(ethylene glycol)-carboxylic acid). The resultant TEM images indicated that the anionic gold nanoparticles preferentially stained the positively charged **CP**$^+$ nanosheets, which confirmed that these nanosheets displayed a positive surface charge (Figure 5A). In contrast, the cationic gold nanoparticles preferentially adsorbed to the surface of the **CP**$^-$ and **CP**$^-$**D**$_3$ nanosheets, which confirmed the presence of a negatively charged surface layer (Figure 5B and D). The anionic gold nanoparticles were observed to surround the **CP**$^-$ nanosheets, probably due to association of excess calcium(II) ions around the edges of sheets. Finally, the surfaces of the triple-layered nanosheet were densely stained with the cationic gold nanoparticles while being essentially devoid of anionic gold nanoparticles under identical conditions (Figure 5C). The incompletely layered structures (concentration ratio of **CP**$^-$/**CP**$^+$ < 2) were observed to interact with both cationic and anionic gold nanoparticles (data not shown). These results implied the presence of both positively and negatively charged domains on the surface of the nanosheets. However, TEM imaging of the nanosheets resulting from the gold nanoparticle binding assays could not generate sufficient contrast to resolve the presence of distinct domains in $x-y$ direction.

The surface charge distributions of the nanosheets were also mapped using ambient electrostatic force microscopy (EFM). EFM images the surface charge distribution that a conductive tip experiences due to electrostatic interactions with a charged substrate. Different charge states on a substrate can be distinguished on the basis of the potential difference with respect to the bias on the tip. This method has been employed in lifted mode to map surface charge within protein[35] and peptide assemblies[36] based on variation of the phase and amplitude response of an AC signal to the surface from the conductive tip. Using a positive scanning tip bias, oppositely charged substrates appear as dark images on a lighter background in EFM amplitude mode and as light images on a darker background in EFM phase mode. For situations in which the interactions between the tip and substrate are electrostatically repulsive, an opposite pattern of signal contrast is observed for the different EFM imaging modes.

EFM scans of **CP**$^+$ nanosheets indicated a repulsive signal in EFM amplitude and phase (Figure 6A), as would be expected for a positively charged substrate interacting with a positively biased tip. In contrast, the EFM images of nanosheets derived from either **CP**$^-$ or **CP**$^-$**D**$_3$ displayed an inverse pattern with respect to that of the **CP**$^+$ nanosheets, which is consistent with an electrostatically attractive interaction between the tip and substrate (Figure 6B and D). The EFM analysis of the triple-layered nanosheets recapitulated the behavior of the negatively charged nanosheets of **CP**$^-$ or **CP**$^-$**D**$_3$ (Figure 6C). Moreover, the EFM signal response of the multilayer sheets was much stronger than any of the single-layer nanosheets, irrespective of the surface charge state. This signal enhancement may be attributed to the thermal stability and greater physical robustness of the multilayered nanosheets. The combined data from EFM image analysis, zeta potential measurements, and charged nanoparticle binding assays are in substantial agreement with a negative surface charge state for the multilayer nanosheets. These observations fully support a mechanism in which the positively charged **CP**$^+$ nanosheets template the assembly of the **CP**$^-$ nanosheets at both exposed surfaces, which results in a triple-layer nanosheet having a compositional distribution of (**CP**$^-$/**CP**$^+$/**CP**$^-$) along the z-direction of the assembly.

Synchrotron SAXS/WAXS measurements provided further evidence of the formation of a triple-layer structure in solution (Figure 7A). Scattering profiles in the Guinier region could be

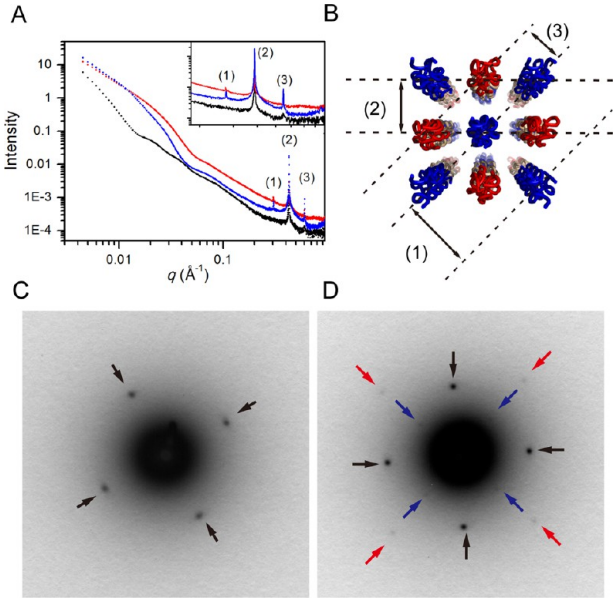

Figure 7. (A) Synchrotron SAXS/WAXS scattering profile for **CP**$^+$ nanosheets (blue), **CP**$^-$ nanosheets with Ca^{2+} (red), and multilayer (**CP**$^-$/**CP**$^+$/**CP**$^-$) nanosheets (black). Inset: expansion of the diffraction peaks. *d*-spacings: (1) 20.6 Å; (2) 14.6 Å; (3) 10.3 Å. (B) Structural model of the tetragonal 2D lattice for the **CP** nanosheets indicating lattice planes associated with the packing of triple helices. The collagen triple helices pack in an antiparallel orientation in which the N-terminal positively charged triads (blue) of one triple helix interact selectively with the C-terminal negatively charged triads (red) of adjacent triple helices. For a more detailed discussion of the contributions of the structural model to the *d*-spacings, see Figure S15 (Supporting Information). (C) Electron diffraction pattern of a **CP**$^+$ nanosheet, with *d*-spacing at 14.2 Å. (D) Electron diffraction pattern of a mature **CP**$^-$/**CP**$^+$/**CP**$^-$ triple-layer nanosheet, with *d*-spacings at 19.6 Å (blue), 14.0 Å (black), and 9.89 Å (red).

fit to a model for sheet-like forms.[37] The Guinier fit for the **CP**$^+$ nanosheet sample afforded a value of 13.3 nm for the average sheet thickness (Figure S9, Supporting Information). The sheet-like structure is also reflected in the oscillating feature in the scattering curve (q up to 0.3 Å^{-1}). However, the oscillation was greatly attenuated and damped due to thickness variation. This thickness variation was estimated as ±3.0 nm through computer simulations (Figure S10, Supporting Information).[2] The thickness calculated from SAXS measurements in solution is greater than the corresponding thickness value of 9.4 nm from AFM height measurements.

The discrepancy between these measurements presumably reflects the difference in the conformation of the charged triad

DOI: 10.1021/jacs.5b03326
J. Am. Chem. Soc. 2015, 137, 7793−7802

extensions in solution versus the solid state. The sheet thickness from AFM measurements closely corresponds to the theoretical thickness for the structured core derived from the **CPII** peptide sequence.[1,2,19] Presumably, the three N-terminal (Pro-Arg-Gly) triads are unstructured and collapsed on the surface of the nanosheets under dry conditions and, therefore, contribute little to the measured height. In solution, the N-terminal $(Pro\text{-}Arg\text{-}Gly)_3$ sequence presumably extends from the surface of the nanosheet in order to promote solvation of the charged amino acid residues. A theoretical limit can be placed on the thickness of the surface layer, which can be correlated with the length of the charged triad extensions in a triple helical conformation. The core thickness of the nanosheet should be ca. 10.3 nm, while the fully extended triads can contribute up to 2.6 nm to each side of the nanosheet (9 residues × 0.286 nm rise/residue).[34] The theoretical sheet thickness of ca. 15.5 nm compares well with the thickness determined from the Guinier analysis, especially in the event that the N-terminal triads may not be fully extended due to the potential for lateral movement on the surface (Figure 1).

A similar situation was observed for the triple-layer sheets, in which the thickness value of 41.4 ± 5.0 nm calculated from the Guinier fit and SAXS curve simulation was significantly larger than the corresponding value of 34 ± 2.0 nm determined from AFM height measurements (Figures S11 and S12, Supporting Information). Again, this larger value can be rationalized on the basis of the contribution of the surface extensions (5.2 nm) to the core thickness of the triple-layered nanosheet (ca. 36 nm). The measured value of the sheet thickness from SAXS analysis (41.4 ± 5.0 nm) agrees quite well with the calculated value based on the structural model (41.2 nm). In contrast, the Guinier fit and SAXS curve simulation for the **CP**$^-$ nanosheets in the presence of calcium nitrate afforded a thickness value of 10.3 ± 2.5 nm (Figures S13 and S14, Supporting Information), which corresponds more closely with the thickness value of 9.9 ± 1.2 nm determined from AFM height measurements than the theoretical value of 15.5 nm for a monolayer sheet with extended (Glu-Hyp-Gly) triads at each surface. This observation suggests that the extended triads may be lying down on the surface of the nanosheet even in the hydrated state, which is presumably due to the coordination of the glutamates by calcium(II) ion.

In addition to form factor scattering, Bragg diffraction peaks were observed for all three nanosheet specimens in the high momentum transfer (q) region of the scattering curve (Figure 7A). Three diffraction peaks were observed for the **CP**$^+$ and **CP**$^-$ nanosheets at q values of 0.305, 0.430, and 0.610 Å^{-1}, which correspond to d-spacings of 20.6, 14.6, and 10.3 Å. These data suggest that the nearest distance between the centers of triple helices corresponds to 14.6 Å. The geometric relationship between these d-spacings can be interpreted in terms of two tetragonal 2D lattices, a dense tetragonal lattice in the middle portion, and a sparse lattice in the top and bottom portions (Figure 7B and Figure S15, Supporting Information). The former contributes to diffraction peaks with d-spacings of 14.6 and 10.3 Å, while the latter contributes to d-spacings of 20.6, 14.6, and 10.3 Å. Bragg diffraction peaks were also observed for the (**CP**$^-$/**CP**$^+$/**CP**$^-$) triple-layer sheets at q values corresponding to d-spacings of 14.6 and 10.3 Å, which coincided with those of the monolayer sheets. The peak at a d-spacing of 20.6 Å is expected to be weak in **CP**$^+$, **CP**$^-$, and **CP**$^-$/**CP**$^+$/**CP**$^-$ nanosheets because the thickness of the sparse lattice at the top and bottom surfaces corresponds to significantly less mass than the core, dense lattice. The absence of the 20.6 Å spacing in the SAXS data for the triple-layer nanosheet was due to a weaker signal, presumably due to a diminished contribution of the sparse surface lattice to the diffraction in comparison to the thicker core lattice.

Electron diffraction (ED) analysis on the nanosheets under dry conditions in the TEM instrument confirmed the tetragonal symmetry of the 2D lattice for the **CP**$^+$ and triple-layer (**CP**$^-$/**CP**$^+$/**CP**$^-$) nanosheets (Figure 7C and D). Sharp diffraction spots were observed at d-spacings of 19.6, 14.0, and 9.89 Å for isolated triple-layer structures, which closely corresponded to the azimuthally averaged lattice spacings determined from SAXS/WAXS measurements. For the **CP**$^+$ nanosheets, a single set of diffraction spots was observed for the major diffraction lattice at a d-spacing of 14.2 Å. The diffraction patterns associated with the other lattice spacings were not observed, presumably due to their weaker intensity and the greater sensitivity to beam damage of the monolayer nanosheets. Four-fold rotational symmetry was observed in all of the electron diffraction patterns, as would be expected for two-dimensional lattices that exhibit tetragonal symmetry. Moreover, the diffraction patterns from the major and minor lattices of the triple-layer nanosheets displayed an angular offset of 45°, which is consistent the proposed symmetry of the 2D lattice.

The SAXS/WAXS measurements and electron diffraction data support a structural model for the **CP**-derived nanosheets that differs from the proposed square 2D lattice of the **NSI** nanosheets.[1] In comparison to the latter system, nanosheets derived from self-assembly of the **CP**$^+$ and **CP**$^-$ peptides display a longer distance (14.6 Å for **CP**$^-$ nanosheets versus 11 Å for the **NSI** nanosheets) for the closest contact between structurally adjacent triple helices in the 2D lattice. This difference in packing density may reflect the different steric requirements necessary to accommodate the 4-(*R*)-aminoproline and arginine residues in a conformation that would maximize stabilizing electrostatic interactions between adjacent triple helices within the 2D lattices of the **NSI** and **CP** nanosheets, respectively. Thus, the structure of the charged residues may represent a design parameter that could be implemented to control the underlying dimensions of the 2D lattice of the nanosheets.

Significantly, the lattice spacings associated with the **CP**$^+$ monolayer nanosheet and (**CP**$^-$/**CP**$^+$/**CP**$^-$) triple-layer nanosheet coincide almost exactly with each other. Thus, the **CP**$^+$ nanosheet can nucleate the controlled growth of the triple-layer nanosheet while preserving the underlying symmetry of the 2D lattice of the template within the nascent layers of **CP**$^-$ peptide. Moreover, CD spectropolarimetric analysis of the triple-layer nanosheets indicates similar thermal stability to the **CP**$^+$ monolayer nanosheets (Figures S16 and S17, Supporting Information), although the transition is significantly broader, perhaps due to the mixed composition of the triple-layer nanosheets. In contrast to the aforementioned results, if the **CP**$^+$ and **CP**$^-$ peptides are mixed and annealed together, structurally and compositionally defined nanosheets are not observed. The CD melting curve is significantly broader than that of the triple-layer nanosheets, presumably as a consequence of compositional and structural heterogeneity (Figure S18, Supporting Information). TEM analysis of the resultant assemblies indicates the presence of unstructured precipitate rather than well-defined nanosheets (Figure S19, Supporting Information).

DOI: 10.1021/jacs.5b03326
J. Am. Chem. Soc. 2015, 137, 7793−7802

CONCLUSION

The fabrication of two-dimensional assemblies presents a significant challenge to current synthetic methods, particularly in terms of structural and compositional control.[13,14] We have described a method, intellectually derived from layer-by-layer assembly,[27] in which nanosheet structures can be fabricated with compositional control along the *z*-direction, while maintaining structural order within the 2D lattice. Two collagen-mimetic peptides, **CP**$^+$ and **CP**$^-$, were designed with macromolecular architectures that comprised asymmetric distributions of charged triad repeats. If these peptides associated into monolayer nanosheets based on the proposed antiparallel packing of collagen triple helices, then the charged triad extensions would be localized on the surfaces of the assembly and available for interaction with the electrostatically and structurally complementary partner peptide. The excess surface charge of the compositionally homogeneous monolayer nanosheets would prevent further association in the *z*-direction and allow the nanosheets to be dispersed in aqueous solution.

The positively charged **CP**$^+$ monolayer nanosheets assemble more rapidly than the negatively charged **CP**$^-$ nanosheets and display greater thermal stability and lateral size. In the absence of calcium ion coordination, the **CP**$^-$ peptide forms small nanosheets over a relatively long incubation period. Therefore, the **CP**$^+$ monolayer sheets provide an ideal template to nucleate further sheet lamination with the **CP**$^-$ peptide. The latent triple helical structure of the charged $(\text{Pro-Arg-Gly})_3$ extensions at the surface of the more stable **CP**$^+$ nanosheet is realized in the presence of the electrostatically complementary **CP**$^-$ peptide. The resultant interfacial interactions promoted the growth of structurally ordered monolayers derived from the **CP**$^-$ peptide at both surfaces of the original **CP**$^+$ nanosheet template. Subsequent growth in the *z*-direction is inhibited due to the excess negative charge present at either surface of the mature assemblies. In theory, further growth of the layered nanostructure could occur by successive addition of positively charged **CP**$^+$ and negatively charged **CP**$^-$ peptides to the triple-layer structure. In practice, the **CP**$^+$ peptide assembles rapidly in the absence of template, which results in a complex mixture of monolayer and multilayer assemblies in the presence of preformed (**CP**$^-$/**CP**$^+$/**CP**$^-$) triple-layer nanosheets.

However, as the self-assembly of the **CP**$^-$**D**$_3$ peptide demonstrates, nanosheet formation can strongly depend on the sequence on the triad extensions, in ways that may be difficult to predict *a priori*. These results suggest that it may be possible to find positively charged amino acids that undergo slow self-assembly into nanosheets. Collagen mimetic peptides that display this self-assembly behavior would be useful substrates for the fabrication of highly laminated nanosheet assemblies with compositional control over an extended length scale in the *z*-dimension. Our experimental results also demonstrate that electrostatic deposition can occur within a given structural context, i.e., the collagen triple helix, which provides a mechanism for assembly of structurally defined 2D nanostructures. This approach has the potential to be extended to peptide-based materials derived from other structural motifs, if suitable noncovalent interactions can be introduced at structurally informed positions within the corresponding amino acid sequence.[11,25,26,38−41]

METHODS

Materials. Chemical reagents were purchased from Sigma-Aldrich Chemical Co. (St. Louis, MO) or Anaspec, Inc. (Fremont, CA), unless otherwise noted. Fmoc-Gly-PEG-PS solid phase synthesis resin was purchased from Applied Biosystems, Inc. (Foster City, CA). Template stripped gold chips were purchased from AMS Biotechnology, LLC. (Cambridge, MA).

Peptide Synthesis. Peptides **CP**$^+$, **CP**$^-$, and **CP**$^-$**D**$_3$ were synthesized as the N-amino, C-acid derivatives on a CEM Liberty microwave-assisted synthesizer using the Fmoc-Gly-PEG-PS resin as the solid support. Standard Fmoc protection chemistry was employed with coupling cycles based on HBTU/DIEA-mediated activation protocols and base induced deprotection (20% piperidine in DMF with 0.1 M HOBt) of the Fmoc group. Crude peptides were purified by reverse-phase HPLC on a C18 column. The target fractions were collected and lyophilized, followed by purity analysis through MALDI mass spectrometry and analytical HPLC (see Figures S20−S25, Supporting Information). Peptides were dialyzed against deionized water (MWCO = 2000 Da) and lyophilized for long-term storage at −20 °C. Peptides were dissolved in MES buffer (20 mM, pH 6.0) at the desired concentration. Solution concentrations were determined from the measured mass of the respective peptides. Samples were thermally annealed at 85 °C for 45 min, and gradually cooled to ambient temperature.

Circular Dichroism Spectropolarimetry. CD measurements were performed on a Jasco J-810 CD spectropolarimeter in 0.10 mm quartz cells using samples prepared at the desired concentration in MES buffer (20 mM, pH 6.0). Spectra were recorded from 300 to 190 nm at a scanning rate of 100 nm/min and a resolution of 0.5 nm. CD melting experiments were performed in the temperature range from 5 to 85 °C at a heating rate of 0.1 °C/min. The intensity of the CD signal at 223 nm was monitored as a function of temperature. Melting temperatures were obtained from the first derivative of the melting curves.

Transmission Electron Microscopy. TEM images were recorded on a Hitachi H7500 microscope with an accelerating voltage of 75 kV. Aqueous peptide solutions were deposited onto 200 mesh carbon coated copper grids (Electron Microscopy Sciences), allowing for 1 min for adsorption of the specimen. Excess liquid was wicked away using filter papers, and the grid was stained with 1% uranyl acetate for 45 s. Excess stain solution was wicked away, and sample grids were dried *in vacuo* prior to TEM measurement.

For the binding assay with gold nanoparticles, the supernatant solution from the nanosheet specimens was exchanged with an equivalent volume of fresh MES buffer (20 mM, pH 6.0) immediately prior to sample preparation in order to remove unassociated peptides. The solutions of either cationic or anionic gold nanoparticles were diluted 10 times using MES buffer (0.5 mM, pH 6.0). An aliquot (8 μL) of the diluted gold nanoparticle solutions was added to the nanosheet solution, which was incubated *in situ* for 30 min at ambient temperature. Specimens were deposited on the EM grids as described above. The sample grids were washed three times using MES buffer (0.5 mM, pH 6.0), air-dried for 30 min, and imaged in the TEM instrument.

Electron Diffraction. Electron diffraction lattice patterns were recorded on the Hitachi H-7500 transmission electron microscope using an accelerating voltage of 40 kV. Specimens were prepared as described above for TEM measurements. A camera length of 1.5 m was employed to expose the small reciprocal lattice. The *d*-spacings were calculated using the equation $d = \lambda L/R$, in which λ is the electron wavelength, L denotes the camera length, and R represents the distances of diffraction signals. An aluminum polycrystalline standard (Ted Pella, Inc.) was used to calibrate the camera length.

Atomic Force Microscopy. Tapping mode AFM scans were performed on a JEOL-4200 instrument, using a silicon AFM tip with a force constant of 5.4−16 N/m. Aqueous solutions of nanosheet specimens in MES buffer (0.5 mM, pH 6.0) were deposited onto a freshly cleaved mica substrate for 5 min, and dried under a flow of nitrogen gas. The *z*-axis was calibrated immediately prior to AFM height measurements using a silicon wafer block test grating with step heights of 20 ± 1 nm (TGZ-20 from Ted Pella, Inc.).

Electrostatic Force Microscopy. The ambient EFM measurements were performed on a Park System XE-100, using Pt−Ir coated,

DOI: 10.1021/jacs.5b03326
J. Am. Chem. Soc. 2015, 137, 7793−7802

electrically conductive cantilevers with a force constant of 2.8 N/m. Aqueous solutions of nanosheets were diluted using MES buffer (0.5 mM, pH 6.0), deposited onto the atomically flat gold substrates (Amsbio, LLC), and air-dried overnight. A +2 V AC bias was applied to the cantilever to map the charge distribution in both EFM amplitude and phase modes.

Zeta Potential Measurements. Zeta potential measurements were obtained on a Malvern Zetasizer Nano Z, equipped with a 4 mW, He−Ne laser at 633 nm. The Zetasizer Nano Z uses the laser Doppler microelectrophoresis to measure zeta potential. Aqueous solutions of nanosheets were diluted to 0.1 mg/mL in MES buffer (20 mM, pH 6.0) at ambient temperature immediately prior to data acquisition.

Small- and Wide-Angle X-ray Scattering Measurements. Synchrotron SAXS/WAXS measurements were performed at the 12-ID-B beamline of Advanced Photon Sources at Argonne National Laboratory, using the methods described previously.[1,2] SAXS/WAXS data were acquired on aqueous solutions of peptide nanosheets at a concentration of 4 mg/mL in MES buffer (20 mM, pH 6.0) at 25 °C. A quartz capillary flow cell (1.5 mm diameter) was employed to prevent radiation damage. Twenty images were collected for each sample and buffer. The 2-D scattering images were converted to 1-D SAXS curves through azimuthally averaging after solid angle correction and then normalizing with the intensity of the transmitted X-ray beam, using the software package at beamline 12ID-B. The 1-D curves of the samples were averaged and subtracted with the background measured from the corresponding buffers. Detailed analysis of the SAXS/WAXS scattering data in terms of a structural model is presented in the Supporting Information (Figures S9−S15).

■ ASSOCIATED CONTENT

Ⓢ Supporting Information

Additional experimental characterization of peptides and peptide assemblies. The Supporting Information is available free of charge on the ACS Publications website at DOI: 10.1021/jacs.5b03326.

■ AUTHOR INFORMATION

Corresponding Author

*vcontic@emory.edu

Notes

The authors declare no competing financial interest.

■ ACKNOWLEDGMENTS

V.P.C. acknowledges financial support from NSF grants CHE-1012620 and CHE-1412580. The authors acknowledge Professor Thomas Orlando for useful discussions. The authors acknowledge Dr. Jnizhi Du for the assistance in the acquisition of the zeta potential data and Sha Li and Yang Liu for providing the gold nanoparticles. This work benefited from the use of the A.P.S. funded by U.S. D.O.E. Office of Basic Energy Sciences, Division of Material Sciences, under contract W-31-109-Eng-38.

■ REFERENCES

(1) Jiang, T.; Xu, C.; Liu, Y.; Liu, Z.; Wall, J. S.; Zuo, X.; Lian, T.; Salaita, K.; Ni, C.; Pochan, D.; Conticello, V. P. *J. Am. Chem. Soc.* **2014**, *136*, 4300−4308.

(2) Jiang, T.; Xu, C.; Zuo, X.; Conticello, V. P. *Angew. Chem., Int. Ed.* **2014**, *53*, 8367−8371.

(3) (a) Przybyla, D. E.; Chmielewski, J. *J. Am. Chem. Soc.* **2010**, *132*, 7866−7867. (b) Przybyla, D. E.; Rubert Pérez, C. M.; Gleaton, J.; Nandwana, V.; Chmielewski, J. *J. Am. Chem. Soc.* **2013**, *135*, 3418−3422.

(4) Hughes, M.; Xu, H.; Frederix, P. W. J. M.; Smith, A. M.; Hunt, N. T.; Tuttle, T.; Kinloch, I. A.; Ulijn, R. V. *Soft Matter* **2011**, *7*, 10032−10038.

(5) Govindaraju, T.; Pandeeswar, M.; Jayaramulu, K.; Jaipuria, G.; Atreya, H. S. *Supramol. Chem.* **2011**, *23*, 487−492.

(6) Hamley, I. W.; Dehsorkhi, A.; Castelletto, V. *Chem. Commun.* **2013**, *49*, 1850−1852.

(7) Xu, F.; Khan, I. J.; McGuinness, K.; Parmar, A. S.; Silva, T.; Murthy, N. S.; Nanda, V. *J. Am. Chem. Soc.* **2013**, *135*, 18762−18765.

(8) Jang, H. S.; Lee, J. H.; Park, Y. S.; Kim, Y. O.; Park, J.; Yang, T. Y.; Jin, K.; Lee, J.; Park, S.; You, J. M.; Jeong, K. W.; Shin, A.; Oh, I. S.; Kwon, M. K.; Kim, Y. I.; Cho, H. H.; Han, H. N.; Kim, Y.; Chang, Y. H.; Paik, S. R.; Nam, K. T.; Lee, Y. S. *Nat. Commun.* **2014**, *5*, 3665.

(9) McGuinness, K.; Khan, I. J.; Nanda, V. *ACS Nano* **2014**, *8*, 12514−12523.

(10) (a) Brodin, J. D.; Ambroggio, X. I.; Tang, C.; Parent, K. N.; Baker, T. S.; Tezcan, F. A. *Nat. Chem.* **2012**, *4*, 375−382. (b) Brodin, J. D.; Carr, J. R.; Sontz, P. A.; Tezcan, F. A. *Proc. Natl. Acad. Sci. U.S.A.* **2014**, *111*, 2897−2902.

(11) (a) Nam, K. T.; Shelby, S. A.; Choi, P. H.; Marciel, A. B.; Chen, R.; Tan, L.; Chu, T. K.; Mesch, R. A.; Lee, B. C.; Connolly, M. D.; Kisielowski, C.; Zuckermann, R. N. *Nat. Mater.* **2010**, *9*, 454−460. (b) Sanii, B.; Kudirka, R.; Cho, A.; Venkateswaran, N.; Olivier, G. K.; Olson, A. M.; Tran, H.; Harada, R. M.; Tan, L.; Zuckermann, R. N. *J. Am. Chem. Soc.* **2011**, *133*, 20808−20815. (c) Kudirka, R.; Tran, H.; Sanii, B.; Nam, K. T.; Choi, P. H.; Venkateswaran, N.; Chen, R.; Whitelam, S.; Zuckermann, R. N. *Biopolymers* **2011**, *96*, 586−595. (d) Robertson, E. J.; Olivier, G. K.; Qian, M.; Proulx, C.; Zuckermann, R. N.; Richmond, G. L. *Proc. Natl. Acad. Sci. U.S.A.* **2014**, *111*, 13284−13289.

(12) Olivier, G. K.; Cho, A.; Sanii, B.; Connolly, M. D.; Tran, H.; Zuckermann, R. N. *ACS Nano* **2013**, *7*, 9276−9286.

(13) Govindaraju, T.; Avinash, M. B. *Nanoscale* **2012**, *4*, 6102−6117.

(14) Ariga, K.; Ji, Q.; Hill, J. P.; Bando, Y.; Aono, M. *NPG Asia Mater.* **2012**, *4*, e17.

(15) (a) Babu, I. R.; Ganesh, K. N. *J. Am. Chem. Soc.* **2001**, *123*, 2079−2080. (b) Umashankara, M.; Babu, I. R.; Ganesh, K. N. *Chem. Commun.* **2003**, 2606−2607.

(16) Siebler, C.; Erdmann, R. S.; Wennemers, H. *Angew. Chem., Int. Ed. Engl.* **2014**, *53*, 10340−10344.

(17) (a) Erdmann, R. S.; Wennemers, H. *Angew. Chem., Int. Ed. Engl.* **2011**, *50*, 6835−6838. (b) Kuemin, M.; Nagel, Y. A.; Schweizer, S.; Monnard, F. W.; Ochsenfeld, C.; Wennemers, H. *Angew. Chem., Int. Ed. Engl.* **2010**, *49*, 6324−6327.

(18) Siebler, C.; Trapp, N.; Wennemers, H. *J. Pept. Sci.* **2015**, *21*, 208−211.

(19) Rele, S.; Song, Y.; Apkarian, R. P.; Qu, Z.; Conticello, V. P.; Chaikof, E. L. *J. Am. Chem. Soc.* **2007**, *129*, 14780−14787.

(20) Ramshaw, J. A.; Shah, N. K.; Brodsky, B. *J. Struct. Biol.* **1998**, *122*, 86−91.

(21) Jalan, A. A.; Hartgerink, J. D. *Curr. Opin. Chem. Biol.* **2013**, *17*, 960−967.

(22) (a) Keshwani, N.; Banerjee, S.; Brodsky, B.; Makhatadze, G. I. *Biophys. J.* **2013**, *105*, 1681−1688. (b) Persikov, A. V.; Ramshaw, J. A.; Kirkpatrick, A.; Brodsky, B. *Biochemistry* **2005**, *44*, 1414−1422. (c) Persikov, A. V.; Ramshaw, J. A.; Kirkpatrick, A.; Brodsky, B. *J. Mol. Biol.* **2002**, *316*, 385−394. (d) Kramer, R. Z.; Venugopal, M. G.; Bella, J.; Mayville, P.; Brodsky, B.; Berman, H. M. *J. Mol. Biol.* **2000**, *301*, 1191−1205. (e) Venugopal, M. G.; Ramshaw, J. A.; Braswell, E.; Zhu, D.; Brodsky, B. *Biochemistry* **1994**, *33*, 7948−7956.

(23) (a) Jalan, A. A.; Demeler, B.; Hartgerink, J. D. *J. Am. Chem. Soc.* **2013**, *135*, 6014−6017. (b) Fallas, J. A.; Hartgerink, J. D. *Nat. Commun.* **2012**, *3*, 1087. (c) Fallas, J. A.; Lee, M. A.; Jalan, A. A.; Hartgerink, J. D. *J. Am. Chem. Soc.* **2012**, *134*, 1430−1433. (d) Fallas, J. A.; Dong, J.; Tao, Y. J.; Hartgerink, J. D. *J. Biol. Chem.* **2012**, *287*, 8039−8047. (e) O'Leary, L. E.; Fallas, J. A.; Hartgerink, J. D. *J. Am. Chem. Soc.* **2011**, *133*, 5432−5443. (f) Russell, L. E.; Fallas, J. A.; Hartgerink, J. D. *J. Am. Chem. Soc.* **2010**, *132*, 3242−3243. (g) Fallas, J. A.; Gauba, V.; Hartgerink, J. D. *J. Biol. Chem.* **2009**, *284*, 26851−26859. (h) Gauba, V.; Hartgerink, J. D. *J. Am. Chem. Soc.* **2008**, *130*, 7509−7515. (i) Gauba, V.; Hartgerink, J. D. *J. Am. Chem. Soc.* **2007**,

DOI: 10.1021/jacs.5b03326
J. Am. Chem. Soc. 2015, 137, 7793−7802

129, 15034−15041. (j) Gauba, V.; Hartgerink, J. D. *J. Am. Chem. Soc.* **2007**, *129*, 2683−2690.
(24) (a) Xu, F.; Silva, T.; Joshi, M.; Zahid, S.; Nanda, V. *J. Biol. Chem.* **2013**, *288*, 31616−31623. (b) Parmar, A. S.; Joshi, M.; Nosker, P. L.; Hasan, N. F.; Nanda, V. *Biomolecules* **2013**, *3*, 986−996. (c) Giddu, S.; Xu, F.; Nanda, V. *Proteins* **2013**, *81*, 386−393. (d) Xu, F.; Zahid, S.; Silva, T.; Nanda, V. *J. Am. Chem. Soc.* **2011**, *133*, 15260−15263. (e) Xu, F.; Zhang, L.; Koder, R. L.; Nanda, V. *Biochemistry* **2010**, *49*, 2307−2316.
(25) (a) Sarkar, B.; O'Leary, L. E.; Hartgerink, J. D. *J. Am. Chem. Soc.* **2014**, *136*, 14417−14424. (b) Jalan, A. A.; Jochim, K. A.; Hartgerink, J. D. *J. Am. Chem. Soc.* **2014**, *136*, 7535−7538. (c) O'Leary, L. E.; Fallas, J. A.; Bakota, E. L.; Kang, M. K.; Hartgerink, J. D. *Nat. Chem.* **2011**, *3*, 821−828.
(26) Xu, F.; Li, J.; Jain, V.; Tu, R. S.; Huang, Q.; Nanda, V. *J. Am. Chem. Soc.* **2012**, *134*, 47−50.
(27) Decher, G. *Science* **1997**, *277*, 1232−1237.
(28) (a) Persikov, A. V.; Ramshaw, J. A.; Brodsky, B. *Biopolymers* **2000**, *55*, 436−450. (b) Chan, V. C.; Ramshaw, J. A.; Kirkpatrick, A.; Beck, K.; Brodsky, B. *J. Biol. Chem.* **1997**, *272*, 31441−31446. (c) Shah, N. K.; Ramshaw, J. A.; Kirkpatrick, A.; Shah, C.; Brodsky, B. *Biochemistry* **1996**, *35*, 10262−10268.
(29) Yang, W.; Chan, V. C.; Kirkpatrick, A.; Ramshaw, J. A.; Brodsky, B. *J. Biol. Chem.* **1997**, *272*, 28837−28840.
(30) Okuyama, K.; Haga, M.; Noguchi, K.; Tanaka, T. *Biopolymers* **2014**, *101*, 1000−1009.
(31) Lumb, R. F.; Martell, A. E. *J. Phys. Chem.* **1953**, *57*, 690−693.
(32) Zhou, Y.; Xue, S.; Yang, J. J. *Metallomics* **2013**, *5*, 29−42.
(33) Okuyama, K.; Kawaguchi, T.; Shimura, M.; Noguchi, K.; Mizuno, K.; Bächinger, H. P. *Biopolymers* **2013**, *99*, 436−447.
(34) (a) Okuyama, K. *Connect. Tissue Res.* **2008**, *49*, 299−310. (b) Okuyama, K.; Xu, X.; Iguchi, M.; Noguchi, K. *Biopolymers* **2006**, *84*, 181−191.
(35) (a) Malvankar, N. S.; Yalcin, S. E.; Tuominen, M. T.; Lovley, D. R. *Nat. Nanotechnol.* **2014**, *9*, 1012−1017. (b) Du, H.; Li, D.; Wang, Y.; Wang, C.; Zhang, D.; Yang, Y. L.; Wang, C. *J. Phys. Chem. B* **2013**, *117*, 9895−9899. (c) Baumann, R. P.; Eussner, J.; Hampp, N. *Phys. Chem. Chem. Phys.* **2011**, *13*, 21375−21382. (d) Oh, Y. J.; Jo, W.; Kim, S.; Park, S.; Kim, Y. S. *Nanotechnology* **2008**, *19*, 365302.
(36) (a) Li, S.; Sidorov, A. N.; Mehta, A. K.; Bisignano, A. J.; Das, D.; Childers, W. S.; Schuler, E.; Jiang, Z.; Orlando, T. M.; Berland, K.; Lynn, D. G. *Biochemistry* **2014**, *53*, 4225−4227. (b) Lee, G.; Lee, W.; Lee, H.; Lee, S. W.; Yoon, D. S.; Eom, K.; Kwon, T. *Appl. Phys. Lett.* **2012**, *101*, 043703. (c) Clausen, C. H.; Dimaki, M.; Panagos, S. P.; Kasotakis, E.; Mitraki, A.; Svendsen, W. E.; Castillo-León, J. *Scanning* **2011**, *33*, 201−207. (d) Clausen, C. H.; Jensen, J.; Castillo, J.; Dimaki, M.; Svendsen, W. E. *Nano Lett.* **2008**, *8*, 4066−4069.
(37) Porod, G. In *Small Angle X-ray Scattering*; Glatter, O., Kratky, O., Eds.; Academic Press: New York, 1982; pp 17−51.
(38) Xu, C.; Liu, R.; Mehta, A. K.; Guerrero-Ferreira, R. C.; Wright, E. R.; Dunin-Horkawicz, S.; Morris, K.; Serpell, L. C.; Zuo, X.; Wall, J. S.; Conticello, V. P. *J. Am. Chem. Soc.* **2013**, *135*, 15565−15578.
(39) (a) Pandya, M. J.; Spooner, G. M.; Sunde, M.; Thorpe, J. R.; Rodger, A.; Woolfson, D. N. *Biochemistry* **2000**, *39*, 8728−8734. (b) Ryadnov, M. G.; Woolfson, D. N. *Nat. Mater.* **2003**, *2*, 329−332. (c) Ryadnov, M. G.; Woolfson, D. N. *Angew. Chem., Int. Ed.* **2003**, *42*, 3021−3023. (d) Papapostolou, D.; Smith, A. M.; Atkins, E. D.; Oliver, S. J.; Ryadnov, M. G.; Serpell, L. C.; Woolfson, D. N. *Proc. Natl. Acad. Sci. U.S.A.* **2007**, *104*, 10853−10858. (e) Sharp, T. H.; Bruning, M.; Mantell, J.; Sessions, R. B.; Thomson, A. R.; Zaccai, N. R.; Brady, R. L.; Verkade, P.; Woolfson, D. N. *Proc. Natl. Acad. Sci. U.S.A.* **2012**, *109*, 13266−13271.
(40) (a) Zhang, S.; Holmes, T.; Lockshin, C.; Rich, A. *Proc. Natl. Acad. Sci. U.S.A.* **1993**, *90*, 3334−3338. (b) Marini, D. M.; Hwang, W.; Lauffenburger, D. A.; Zhang, S.; Kamm, R. D. *Nano Lett.* **2002**, *2*, 295−299.
(41) Swanekamp, R. J.; DiMaio, J. T.; Bowerman, C. J.; Nilsson, B. L. *J. Am. Chem. Soc.* **2012**, *134*, 5556−5559.

DOI: 10.1021/jacs.5b03326
J. Am. Chem. Soc. 2015, 137, 7793−7802